The role of tungsten species in the transition of anodic nanopores to nanotubes formed on iron alloyed with tungsten

Laras Fadillah[a], Kentaro Takase,[b] Hikaru Kobayashi,[b] Sylwia Turczyniak-Surdacka,[c] Marcin Strawski,[c] Damian Kowalski,*[,b,c] Chunyu Zhu[b], Yoshitaka Aoki[b], Hiroki Habazaki*[,b]

[a]*Graduate School of Chemical Sciences and Engineering, Hokkaido University, Kita-Ku Kita 13, Jo Nishi 8, Sapporo, Hokkaido 060-8628, Japan*

[b]*Division of Applied Chemistry, Faculty of Engineering, Hokkaido University, Kita-Ku Kita 13, Jo Nishi 8, Sapporo, Hokkaido 060-8628, Japan*

[c]*Faculty of Chemistry and Biological and Chemical Research Centre, University of Warsaw, Zwirki i Wigury 101, 02-089 Warsaw, Poland*

Keywords: anodizing, iron oxide, nanotubes, anodic oxide

*damian.kowalski@chem.uw.edu.pl
*habazaki@eng.hokudai.ac.jp

Abstract

The effect of alloying of sputter-deposited Fe with 9 at.% tungsten on the growth of nanoporous anodic oxide was studied in ethylene glycol electrolyte containing 0.1 mol dm^{-3} ammonium fluoride and 1.5 mol dm^{-3} water. The classic nanoporous anodic film (Al_2O_3-like) was developed on pure Fe while the transition of nanopores to nanotubes (TiO_2-like) was observed for anodizing of Fe-W alloy. The pores/nanotubes having average diameter 50-110 nm and 30-60 nm on pure Fe and Fe-W alloy anodized at voltage 40-60 V, respectively. Both nanoporous/nanotubular anodic films grow in line with the field assisted flow model with a few fundamental details: i) transition of nanopores to nanotubes is observed upon anodizing of Fe-W alloy, ii) significant reduction of the cell size (nanotube diameter) is obtained on Fe-W alloy, iii) relatively thick layer is produced at Fe-W

alloy/oxide interface. The primary reason of this transition to nanotubes as well as chemical changes is discussed in view of effective modification of the cell boundary region with tungsten species, probably WF_6 compound, upon growth of anodic film under influence of high electric field strength. The possible reason of developing the space in between nanotubes is faster kinetics of WF_6 reaction with water over the presence of low solubility FeF_x species. Alloying of iron is one of the effective ways to modify the nanostructure of the anodic film on iron.

1. Introduction

Anodizing is a high voltage electrochemical conversion process that forms barrier-type oxide layers or self-organized nanoporous/nanotubular structures. So far, the Al_2O_3-like nanopores and TiO_2-like nanotubes could be successfully synthesized on valve metals and alloys such as tantalum, niobium, zirconium, hafnium, etc [1]. Very recently, the formation of self-organized nanoporous and nanotubular anodic films has also been reported on non-valve metals, including iron and stainless steel [2-9]. The surface modification of iron and its alloys is highly demanded in view of its essential role in the field of corrosion and large steel construction market [10]. In addition to corrosion resistance of iron alloys, the surface modifications are necessary to provide additional functionalities such as superhydrophobic and superoleophobic properties for anti-ice and anti-snow sticking, self-cleaning, anti-fouling, etc [11].

Anodizing of iron is practically more complex in processing in relation to other valve metals such as Ti, Ta, Nb, etc., due to difficulty of keeping the passive sate of iron. Growth of porous anodic film is therefore not favored in aqueous electrolytes since at high potential, formation of soluble ferrate ions is promoted [12, 13] as well as anodic gas generation. The key for growth of thick porous anodic layer on iron is therefore good control over the passivity/corrosion which can be effectively provided in organic electrolytes containing small amounts of water and fluorides. The morphology

of the anodic layer is mainly controlled by the voltage/current in the anodizing process. In ethylene glycol electrolyte containing 0.1 mol dm^{-3} ammonium fluoride and 1.5 mol dm^{-3} water, the nanopores (Al_2O_3-like) and nanotubes (TiO_2-like) can be formed on iron. The nanoporous-type anodic film is preferentially formed on iron, possibly due to relatively slow kinetics of dissolution of fluoride-enriched cell boundary regions [8]. The partial transition of nanopores to nanotubes is typically observed at enhanced voltages/currents. The primary reason of this transition is formation of fluoride rich layer at metal/anodic-film interface [14] and its transfer to the cell boundary region, once the porous film grows by field assisted plastic flow [8]. Although the formation of nanopores on aluminum is quite well understood, some features of the nanotubular film formation are still the subject of debate.

The insight into the growth mechanism may be achieved by tracer studies as demonstrated for the alumina case by using ^{18}O isotope tracer technique [15]. The key data obtained by means of the nuclear microanalysis is the information on the contribution of oxygen transport in the growing of the film and therefore direct indication on relative ratio of film formed at metal/oxide interface to that formed at oxide electrolyte interface. It was demonstrated that both Al^{3+} and O^{2-} ions migrate in anodic alumina, with 40% of the ionic current carried by the aluminum ions while about 60% transported by oxygen anions. The pore formation resulted from the loss of aluminum cations to the electrolyte with reduced growth efficiency close to 60% for porous film [15]. A number of information related to growth mechanism were obtained by introducing W tracer into the structure of anodic film by Garcia-Vergara et al [16-22]. The mechanical stress essentially triggered by electrostriction forces and change of the oxide volume ratio described by Pilling–Bedworth ratio is presumed to be responsible for the flow of film material from pore base to pore wall and hence the formation of pores [23]. Based on the tungsten tracer studies, the mechanism of pore generation and

development in porous anodic alumina films was explained by flow mechanism based on direct experimental evidences. Plastic flow of alumina beneath the pore in the presence of ion transport and comprehensive stresses displaces the material from the barrier layer towards the cell wall region, and is predicted to contribute to an increased thickness of porous film relative to that of metal consumed. The STEM observation showed that tungsten band is distorted, flowing upward toward the cell wall regions from the pore base as pore develops. These results indicate the flow of film material owing to the plasticity and high compressive stresses in barrier layer of porous anodic films.

In the present study, the anodizing of Fe-W alloy was studied for the first time. The results were compared with that of anodizing of pure Fe for a better understanding the growth mechanism of the anodic films. Moreover, the influence of operating conditions, especially anodizing voltage on the geometry of nanopores including pore diameter, was analyzed. The primary interest in this study was to examine the influence of tungsten on the growth process as well as chemical changes of formed oxide.

2. Experimental

Magnetron-sputtered Fe and Fe-W (9 at.%) films having the thickness of approximately 450 nm were used for anodizing. The target consisted of 99.99 % pure iron disk of 100 mm in diameter and one 99.9 % tungsten disk of 20 mm in diameter placed on the sputter erosion region of the iron disk. Sputter deposition was carried out in 99.999% pure argon atmosphere at 2.5×10^{-3} Torr with the current 0.5 A and voltage 350 V for 15 min. The composition of the alloy was evaluated by electron probe micro analyzer (EPMA) and equaled to 9 at.% tungsten.

The Fe and Fe-W alloys were anodized at 40-60 V for 300 s in ethylene glycol electrolyte containing 0.1 mol dm^{-3} ammonium fluoride and 1.5 mol dm^{-3} deionized water at room temperature in o-ring type cell with a two-electrode system using platinum counter electrode without stirring of

electrolyte. After anodizing, the specimens were rinsed in ethylene glycol, ethanol, and then dried in nitrogen stream.

The surface morphology and cross sections of the specimens were examined by a Zeiss Sigma 500 field emission scanning electron microscope (SEM) instrument. Elemental depth profiles of the specimens were obtained by a Horiba Jobin Yvon 5000 RF glow discharge optical emission spectrometer (GDOES) in neon atmosphere at 800 Pa by applying 35 W RF power under a pulse mode. The data were recorded at a sampling interval 0.02 s. The diameter of sputtered area was 4 mm. The cross-sections of anodic films were examined by a JEOL, JEM-ARM200F scanning transmission electron microscope (STEM) with energy dispersive X-ray spectrometry (EDS) facilities. Electron-transparent sections were prepared by a Hitachi FB-2100 focused ion beam (FIB) system employing a Ga^+ ion beam. X-ray photoelectron spectroscopy (XPS) spectra were acquired using a Kratos Axis Supra spectrometer, equipped with a monochromatic Al Kα radiation (1486.7 eV) source. The instrument work function was calibrated to give a BE of 84.0 eV ± 0.1 eV for the $4f_{7/2}$ line of metallic gold and the spectrometer dispersion was adjusted to give a BE of 932.62 eV for the Cu $2p_{3/2}$ line of metallic copper. Energy resolution was examined on silver sample. Survey (wide) spectra were collected with a quality corresponding to the full width at half maximum (FWHM) parameter for Ag 3d line equal to 0.71 eV at energy step size equal to 0.5 eV. For high resolution spectra the FWHM parameter for Ag 3d line was equal to 0.58 eV at step size was: 0.1 eV. Kratos charge neutralizer system was used to reduce charge compensation. The peaks fitting was conducted using CasaXPS software version 2.3.18 on a Shirley background. All spectra were calibrated using the adventitious C 1s peak with a fixed value of 285.0 eV. The in-depth composition of the films was probed by using secondary-ion mass spectroscopy (SIMS). As-received samples were transferred without special pre-treatment to the analytical chamber where the pressure was 7×10^{-10} Torr. Distribution of elements was obtained with a time-of-flight SIMS

apparatus (TOF SIMS 5, ION-TOF GmbH) operating in dual beam mode. Samples were sputtered by Cs^+ ions (2 keV, 135 nA), rastered over 320 μm by 320 μm area. Exposed this way, internal layers of films were analyzed with use of Bi^+ ions (at 64 μm by 64 μm central region only). The primary ion (target) current was typically 1.2 pA. Low energy electron flood gun was used to reduce sample charging during analysis. The internal mass calibration was performed using several ions from the mass range starting from C^- up to $W_2O_6^-$.

3. Results and Discussion

j-t curves and morphology of anodic films

Anodizing of sputter-deposited Fe and Fe-W (9 at.%) alloy was performed at a constant voltage between 40 V and 60 V in ethylene glycol electrolyte containing 1.5 mol dm^{-3} water and 0.1 mol dm^{-3} NH_4F at room temperature for 300 s. Figure 1 shows the current-time (*j*-*t*) transients obtained during anodizing of both specimens. Two distinct stages are clearly visible on *j*-*t* curves; the first stage of anodizing, observed within the first tens of seconds is characterized by rapid current drop and is typically associated with initial formation of barrier-type oxide at the alloy electrolyte interface [1] and possible pore initiation. The second stage of anodizing is a quasi-steady state where the current density is nearly constant. The time scale for the stage I is independent of the applied voltage, but the magnitude of current drop slightly increases with anodizing voltage. The current drop in stage I region is seven times faster for Fe-W alloy than that for pure Fe so that a quasi-steady state anodizing condition is more rapidly established on the Fe-W alloy. An initial anodizing stage is more distinct by plotting *i*-*t* curves in the logarithmic scale [24, 25]. This is apparent when one looks at the *j*-log*t* graph (Fig. 1) and compares charge passed during the first stage of anodizing of 2.2 and 0.9 C cm^{-2} for Fe and Fe-W, respectively, estimated at 40 V where the contribution of oxygen

evolution reaction, involved during anodizing of Fe and Fe-W alloy in this electrolyte, is significantly reduced [8]. During anodizing of Fe and Fe-W alloy, oxygen evolution was observed by naked eye for anodizing at 60 V and became less significant at lower voltages. The shape of *j-t* curve for Fe in Fig. 1a strongly depends on the applied voltage and is characterized by a steady state current density at 40 V while the current density gradually increases at 50 and 60 V probably due to Joule heat effect [8]. The current density for anodized Fe-W alloy in Fig. 1b is slightly higher than the current density for pure Fe in Fig. 1a due to the higher electric field applied over a thinner barrier layer formed on Fe-W alloy as discussed later. The total charge passed during 300 s anodizing of Fe and Fe-W at 40 V equals to 10 and 12 C cm^{-2}, respectively. The current drop observed during last 20 s of anodizing of Fe-W alloy at 60 V results from consumption of the alloy above glass substrate and subsequent narrowing of the surface area available for oxidation of Fe-W, having negligible effect on the final structure.

The cross-section SEM images for Fe-W alloys anodized at 40-60 V for 300 s are demonstrated in Fig. 2 with an anodic layer formed on pure Fe at 60 V shown as a reference. The thickness of anodic layer varies with applied voltage and equals 0.98, 1.28 and 1.76 μm for alloy anodized at 40, 50 and 60 V, respectively, aligned with higher electric field at higher anodizing voltage. The thickness variations correlate very well with the applied total electric charge (Q_t) of 12, 15 and 20 C cm^{-2} upon anodizing at 40, 50 and 60 V, respectively. This suggests that the enhanced oxygen gas generation observed at higher anodizing voltage is due to the increased current density, not the increased current efficiency for gas generation. Anodizing of Fe-W alloy at 60 V results in formation of 1.76 μm thick anodic layer which is approximately the same as anodic film formed on pure Fe shown as a reference in Fig. 2. The total electric charge of 17 C cm^{-2} is required for anodic film development on pure Fe which is 15% less than that for Fe-W case at the same anodizing conditions. The slight difference in Q_t value may be related to the thickness/morphology changes and/or oxygen

evolution reaction aspects.

The classic Al_2O_3-like nanopores are developed on pure Fe as expected for short anodizing time and relatively low voltage impacts according to the previous study [8]. The detailed analysis of the anodic layer formed on Fe-W alloy uncovers the shape of TiO_2-like nanotubes (Fig. 2). The inset of SEM image of Fe-W alloy at 60 V in Fig. 2 shows that the bottom part of the anodic film is composed of the array of nanotubes.

The surface morphology of nanoporous/nanotubular anodic film formed by anodizing of pure Fe and Fe-W alloy at 40-60 V is shown in Fig. 3. The microstructure of the as-deposited substrate surface (Fig. 3 a,e) has an impact on the surface morphology and self-organization of pores/tubes particularly observed at lower anodizing voltages for Fe-W case where the formed nanopores/nanotubes are organized along the longitudinal grains (Fig. 3 f-h). Such arrangement can be clearly understood in terms of preferential nucleation of the pores in the dimples [26] of the textured alloy which slightly differs from that of pure Fe. The pore diameter linearly increases with anodizing voltage 40-60 V from 50 to 110 nm and from 30 to 60 nm for anodic film formed on pure Fe and Fe-W alloy, respectively (Fig. 3). The effective cell size reduction is therefore observed with alloying of the iron with tungsten.

Composition of anodic films

Figure 4a,b shows GDOES elemental depth profiles, displaying the change in the optical emission intensities from oxygen, iron, fluorine and tungsten with the time of sputtering for Fe and Fe-W anodized at 60 V. The depth distribution of Fe, W and O clearly identifies the interface between alloy and formed anodic film. The total time required to sputter through the thickness of the porous anodic film is approximately 22 and 54 s for pure Fe and Fe-W alloy, respectively, resulting mainly from different sputtering rates of Fe and W. The GDOES depth profile revealed the incorporation of fluorine species from electrolyte and their distribution in anodic layer strongly depending on alloying

element. The enrichment of fluoride in porous anodic film immediately above the metal/film interface formed on pure Fe should be associated with faster migration of F^- ions relative to that of O^{2-} ions under the high electric field during film growth [14]. The accumulation of fluorides at the metal/oxide interface for pure Fe case is evident from high resolution STEM/EDS mapping studies shown in a previous study [8]. The essential difference in the element distribution for porous films developed on Fe and Fe-W alloy is the unusual distribution of fluorine, *i.e.* the absence of F peak at alloy/oxide interface for Fe-W system. Another interesting feature for anodic film developed on Fe-W alloy is the presence of oxygen peak at the first 10 s of sputtering time suggesting modification of surface region, both discussed in the next section of this paper.

The qualitative analysis of the surfaces for Fe and Fe-W alloy anodized at 60 V was performed based on the XPS wide scan spectra. Results allowed to confirm that the nanoporous/nanotubular anodic films contained Fe, W, F, C and O elements (ESI). The high-resolution Fe 2p region spectra of anodic films formed on Fe and Fe-W, shown in Fig. 5 a,b (ESI), consist of two peaks assigned to the Fe $2p_{3/2}$ and Fe $2p_{1/2}$ spin-orbits components (Δ = 13.2 eV). Iron oxidation state was examined by curve-fitting the Fe $2p_{3/2}$ region with two well resolved components located at 711.3 and 714.2 eV. The resulting fit suggests coexistence of Fe(II) and Fe(III) oxidation states. The relative concentration of these two components has not been determined since Fe 2p region overlaps with F 1s plasmons, however, the shoulder at 714.2 eV is more pronounced for anodic porous film formed on pure Fe. According to literature data, analysis of the lower binding energy peak is not unequivocal. This peak can be related to the presence of Fe(II) in FeF_2 [27-29], however, Fe(III) in Fe_2O_3 and FeOOH were also reported close to this position [29, 30]. So far, published results revealed that signal around 710 eV suggests the existence of FeO, therefore the presence of FeO cannot be excluded. The peak at energy even higher than 714.2 eV, which was found in this work, is assigned to the FeF_3 [27, 28]. In addition, binding energy of F 1s (648.8±0.2 eV) and its

symmetrical shape is in accordance with the literature given for metal fluoride [27, 28, 31]. The presence of FeF_x is consistent with identification of fluoride-rich-layer by Shahzad et al. [8] by means of STEM/EDS elemental mapping in the transition of anodic nanopores to nanotubes formed on bulk iron. The primary location of FeF_x is the cell boundary and oxide/metal interface [8]. In the XPS spectrum a very intense signal of O 1s region was recorded. The spectrum can be resolved into two peaks for anodic Fe or three peaks for anodic Fe-W. The high binding energy component O 1s (532.0 eV) recorded for anodic Fe is related to the presence of organic impurities, which is confirmed in C 1s region (signal from C-O, C-O-C, C-C=O, carbonates). The other peak, at 530.3 eV comes from lattice oxygen which confirm the presence of Fe_xO_y. The position of this peak slightly shifts into higher binding energy (530.5 eV) after addition of tungsten, which is similar to the O 1s values for WO_3 [32]. Additionally, 531.7 and 533.5 eV appear. High binding energy peaks can be assigned, like previously, to the presence of organic and adsorbed water, respectively. Based on the W 4f region it can be excluded that the peak around 531.7 eV is related to the presence of WO_{3-x} phase, caused by the existence of hydroxyl groups on the surface. The W 4f has well separated spin-orbit components (Δ=2.15 eV). The position of W $4f_{7/2}$ (35.8 eV) and its symmetrical shape suggest presence of only WO_3 phase [33-35].

ToF-SIMS mass spectra, cumulated during the depth profiling measurement, were acquired in negative mode to avoid the influence by an external oxygen source (Fig. 5 c,d). The spectra show many components which can be assigned to the iron oxides, iron fluorides, tungsten oxides and tungsten oxide fluorides ion fragments. For detailed analysis the 225-325 m/z region was chosen as the most characteristic ions produced at the sample surface are WO_x clusters [36]. Anodizing of tungsten or its alloys typically results in formation of WO_3 domains in anodic film structure [37, 38]. The complexity of the spectrum is affected by the presence of oxide-fluoride forms. Tungsten has five isotopes of which four are present in the predominant quantity and relatively similar amount.

This isotopic fingerprint allowed us to distinguish the contribution of individual fragments from groups of peaks that occurs at 230, 246, 271 and 293 m/z values. Figure 5c shows that WO_3^- and various $WO_xF_y^-$, such as WOF_4^- and $WO_2F_2^-$, could be assigned. Since WF_6 form was our main point of interest a zoomed data at 292.5-300.5 m/z range is given in Fig. 5d proving that WF_6 molecule is present in the film structure. The depth profile experiment allowed to monitor the content of above fragments in the nanotubular film structure. Figure 5e shows that various fluorides forms are stable among the film depth. A typical behavior for ToF-SIMS measurements in the depth profiling mode is the stabilization of the etching process, therefore, the content of individual fragments in the first stage undergo non-specific changes during the first 60 s. It is obvious that the only component that intensity change differs from the other fragments is WF_6^-. A clear disappearance of this component in the near-surface region is visible. We assume that this part of the film has been exposed to air/water and this reactive compound has decomposed as discussed in the next section of the paper.

Analysis of film by STEM

The scanning transmission electron micrograph (STEM) of a FIB lamella for Fe-W alloy anodized at 60 V is shown in Fig. 6. The shape of nanotubes is evident from high angle annular dark field (HAADF) images. The thickness of the anodic film is approximately 1.7 μm with the inner nanotube diameter of 60 nm, consistent with previous SEM observations. The regions with lighter appearance on STEM micrograph (Fig. 6b) are corresponding to nanotube walls composed of mixed tungsten/iron oxide containing fluorides. Relatively thick layer at the alloy/oxide interface was detected (Fig. 6c). Its thickness varies across the FIB lamella from 40-130 nm as demonstrated in low resolution STEM image (Fig. 6d). Such large thickness variations cannot be caused by electrochemical reaction as the high electric field is primarily localized in the barrier-layer forming uniform anodic layer depending on the applied voltage. Those thickness variations supported by

unusual GDOES elemental depth distribution suggest chemical nature of its formation.

Growth of nanoporous/nanotubular anodic films

The above findings reveal that alloying of iron with 9 at.% of tungsten results in structural changes upon anodizing in ethylene glycol electrolyte containing 1.5 mol dm^{-3} water and 0.1 mol dm^{-3} ammonium fluoride. Essentially, two types of anodic structures are observed: Al_2O_3-like nanopores developed on pure Fe, and TiO_2-like nanotubes developed on Fe-W alloy. Schematic illustration of formed structures is demonstrated in Fig. 7.

Two fundamental mechanisms have been proposed for formation of nanoporous/nanotubular anodic films: i) field assisted dissolution model, [39] and ii) field assisted flow model [20, 22, 40]. Very recently Shahzad et al. showed that porous anodic film on iron may grow according to both models critically depending on the water concentration in electrolyte [8]. In the classic field assisted dissolution model the thickness of barrier-layer between metal and porous layer is kept constant under constant voltage. The formed structure is typically characterized by i) presence of less organized nanopores, ii) thick barrier-layer, and iii) flat metal/oxide interface. In the field assisted flow model, which was proposed using tungsten tracer studies [21, 22, 40, 41], the resulting structure is typically characterized by i) presence of nanopores or nanotubes with high degree of self-organization, ii) thin barrier layer, iii) scalloped metal/oxide interface.

The key mechanism for the growth of anodic film on Fe-W alloy is the field assisted flow model, as only the plastic flow may rearrange the initial horizontal position of anodic layers into vertical position and therefore develop nanotube with the composition of the -outer and -inner shell corresponding to -bottom and -top of the barrier layer, respectively [1]. The general growth is analogous to that formed on pure Fe in electrolyte containing 1.5 mol dm^{-3} water [8] except a few fundamental aspects: i) the transition of nanopores to nanotubes is observed by alloying with

tungsten, ii) significant reduction of the cell size (nanotube diameter) is obtained on Fe-W alloy, iii) relatively thick layer is produced at alloy/oxide interface.

The nanotubes instead of nanopores are considered to be formed due to faster kinetics of WF_6 (or similar compound) dissolution. WF_6 domains and their decomposed forms have been detected on ToF-SIMS mass spectra in the nanotubular film (Fig. 5). Taking into account fast inward-migration of F^- [14] and very slow outward-migration of W^{6+} species [37] in anodic film, the primary location of WF_6 compound should be the bottom of barrier-layer which is switched to the cell boundary position due to stress generated at the barrier-layer and material flow according to the field assisted flow model as discussed above. The difficulty in detection of WF_6 is its decomposition due to hydrolysis reaction [42] in contrast to FeF_2 which has low solubility constant of $8.3x10^{-3}$ mol dm^{-3} [43]. WF_6 is generally considered to be a gas at standard conditions [42, 44], however, may be stabilized by the oxide structure as the WF_6 domains and their decomposed forms, have been identified by ToF-SIMS analysis. Its distribution in the depth (Fig. 5e) suggest faster decomposition in near surface region of the nanotubular layer. Whereas WF_6 has been identified in the film structure, it is not completely understood if the compound is entirely transformed to oxide structure or partially evolved as a gas during anodizing process. In any case, the primary consequence of alloying of iron with tungsten is modification of the cell boundary region and full transition to nanotubes as observed on SEM and STEM images.

The cell size, which is corresponding to the developed nanotube diameter, is effectively modified by alloying element as demonstrated in Fig. 8. The reduction of cell size may be understood as an effect of thinner barrier layer formed on Fe-W alloy during the initial growth as observed in stage I of the *i-t* curves in Fig. 1 and therefore development of smaller pore/tube cells by means of horizontal to vertical oxide reorganization due to material flow effect. Since the same voltage is applied, over

a thinner barrier layer on Fe-W, to some extent a stronger electric field may be applied leading to morphological alternations.

The origin of a thick layer formed at metal/nanotubular-film interface observed on STEM image (Fig. 6a) may be misidentified and at first glance could suggests that alloying of iron with tungsten leads to change of growth mechanism from flow model into field assisted dissolution model as similar barrier layers are formed. The clear shape of developed nanotubes is however against that concept and suggests another origin of its formation. Variations in thickness of this layer 40-130 nm (Fig. 6d) suggests chemical nature of formation since electric filed located in barrier layer produces homogeneous layers of regular structure and thickness. The possible reason of the layer formation would be post reaction of WF_6 or similar compound remaining at the bottom of nanostructure, with moisture after completed anodizing process. WF_6 is typically unstable and easily hydrolyze with water though three elementary steps (1-3):

$$WF_6 + H_2O \rightarrow WOF_4 + 2HF \quad (1)$$

$$WOF_4 + H_2O \rightarrow WO_2F_2 + 2HF \quad (2)$$

$$WO_2F_2 + H_2O \rightarrow WO_3 + 2HF \quad (3)$$

The overall reaction is $WF_6 + 3H_2O = WO_3 + 6HF$ where 1 mol dm^{-3} WF_6 produces 6 mol dm^{-3} hydrofluoric acid. Such harsh acidic conditions may drive chemical reaction with alloy at anodic film base, and therefore thickening the layer at the alloy/nanotubular-film interface as demonstrated in Fig 6c. The absence of characteristic fluorine peak in the GDOES depth profile, in contrast to that for pure Fe case (Fig. 4), at alloy/nanotubular-film interface and consequently uniform distribution of fluorides suggest that originally formed fluoride rich layer is consumed in post reaction process. The fluoride rich layer, FeF_x formed on pure iron is practically free of oxygen species as

demonstrated elsewhere [8]. The composition of the layer obtained by STEM/EDS analysis on Fe-W alloy shows 17.2, 3.4, 35.4 and 44.0 at.% for Fe, W, F and O, respectively, indicating rather complex structure of the layer containing compounds such as metal oxides and metal oxyfluorides as a result of post reaction.

4. Conclusions

The present study shows that alloying of iron with 9 at.% tungsten has meaningful implications on the growth and resulting structure of anodic film. Based on the results obtained the following conclusions can be drawn:

(i) Alloying of iron with 9 at.% of tungsten results in transition of nanoporous oxide to nanotubular nanostructure. The possible reason of this transition is faster kinetics of WF_6 reaction with water over the presence of low solubility FeF_x species, easily developing the space in between nanotubes.

(ii) The pore size of the anodic films on the Fe-W alloy is smaller than that on pure Fe and the quasi-steady state anodizing condition is more rapidly established on the Fe-W alloy. Such influences of alloying with tungsten are most likely due to formation of thinner barrier layer formed on the Fe-W alloy.

(iii) The anodic nanopores developed on pure Fe and anodic nanotubes developed on Fe-W alloy composed of Fe_xO_y and WO_3 domains grow in line with the field assisted flow model. The thick layer formed at the alloy/oxide interface is possibly a result of chemical reaction due to exposition of structure to moisture.

Acknowledgements

The present study was supported in part by JFE 21st Century Foundation. A part of this study was conducted at Hokkaido University Microstructure Characterization Platform supported by Ministry of Education, Culture, Sports, Science and Technology (MEXT), Japan. D.K. would like to acknowledge for financial support from National Science Centre grant number 2013/11/B/ST4/02151. ToF-SIMS and XPS studies were carried out with the equipment purchased by Biological and Chemical Research Centre, University of Warsaw, established within the project co-financed by European Union from the European Regional Development Fund under the Operational Programme Innovative Economy, 2007–2013.

References

[1] D. Kowalski, D. Kim, P. Schmuki, TiO2 nanotubes, nanochannels and mesosponge: Self-organized formation and applications, Nano Today, 8 (2013) 235-264.
[2] H.E. Prakasam, O.K. Varghese, M. Paulose, G.K. Mor, C.A. Grimes, Synthesis and photoelectrochemical properties of nanoporous iron (III) oxide by potentiostatic anodization, Nanotechnol., 17 (2006) 4285-4291.
[3] S.K. Mohapatra, S.E. John, S. Banerjee, M. Misra, Water Photooxidation by Smooth and Ultrathin alpha-Fe2O3 Nanotube Arrays, Chem. Mater., 21 (2009) 3048-3055.
[4] H. Habazaki, Y. Konno, Y. Aoki, P. Skeldon, G.E. Thompson, Galvanostatic Growth of Nanoporous Anodic Films on Iron in Ammonium Fluoride-Ethylene Glycol Electrolytes with Different Water Contents, Journal of Physical Chemistry C, 114 (2010) 18853-18859.
[5] Y. Konno, E. Tsuji, P. Skeldon, G.E. Thompson, H. Habazaki, Factors influencing the growth behaviour of nanoporous anodic films on iron under galvanostatic anodizing, J. Solid State Electrochem., 16 (2012) 3887-3896.
[6] K. Kure, Y. Konno, E. Tsuji, P. Skeldon, G.E. Thompson, H. Habazaki, Formation of self-organized nanoporous anodic films on Type 304 stainless steel, Electrochem. Commun., 21 (2012) 1-4.
[7] H. Tsuchiya, T. Suzumura, Y. Terada, S. Fujimoto, Formation of self-organized pores on type 316 stainless steel in organic solvents, Electrochim. Acta, 82 (2012) 333-338.
[8] K. Shahzad, D. Kowalski, C.Y. Zhu, Y. Aoki, H. Habazaki, Ex Situ Evidence for the Role of a Fluoride-Rich Layer Switching the Growth of Nanopores to Nanotubes: A Missing Piece of the Anodizing Puzzle, Chemelectrochem, 5 (2018) 610-618.
[9] S.P. Albu, A. Ghicov, P. Schmuki, High aspect ratio, self-ordered iron oxide nanopores formed

by anoclization of Fe in ethylene glycol/NH4F electrolytes, Phys. Status Solidi RRL, 3 (2009) 64-66.
[10] N. Sato, Toward a more fundamental understanding of corrosion processes, Corrosion, 45 (1989) 354-368.
[11] A. Kasuga, A. Koyama, K. Nakayama, D. Kowalski, C. Zhu, Y. Aoki, H. Habazaki, Fabrication of Superoleophobic Surface on Stainless Steel by Hierarchical Surface Roughening and Organic Coating, ISIJ Int., advpub (2018).
[12] F. Beck, R. Kaus, M. Oberst, Transpassive Dissolution of Iron to Ferrate (Vi) in Concentrated Alkali Hydroxide Solutions, Electrochim. Acta, 30 (1985) 173-183.
[13] M. Pourbaix, Atlas of Electrochemical Equilibria in Aqueous Solutions, NACE, Houston, 1974.
[14] H. Habazaki, K. Fushimi, K. Shimizu, P. Skeldon, G.E. Thompson, Fast migration of fluoride ions in growing anodic titanium oxide, Electrochem. Commun., 9 (2007) 1222-1227.
[15] C. Cherki, J. Siejka, Study by Nuclear Microanalysis and O-18 Tracer Techniques of Oxygen-Transport Processes and Growth Laws for Porous Anodic Oxide Layers on Aluminum, J. Electrochem. Soc., 120 (1973) 784-791.
[16] S.J. Garcia-Vergara, H. Habazaki, P. Skeldon, G.E. Thompson, Tracer studies relating to alloying element behaviour in porous anodic alumina formed in phosphoric acid, Electrochim. Acta, 55 (2010) 3175-3184.
[17] S.J. Garcia-Vergara, D. Le Clere, T. Hashimoto, H. Habazaki, R. Skeldon, G.E. Thompson, Optimized observation of tungsten tracers for investigation of formation of porous anodic alumina, Electrochim. Acta, 54 (2009) 6403-6411.
[18] S.J. Garcia-Vergara, P. Skeldon, G.E. Thompson, H. Habazaki, Behaviour of a fast migrating cation species in porous anodic alumina, Corros. Sci., 50 (2008) 3179-3184.
[19] S.J. Garcia-Vergara, P. Skeldon, G.E. Thompson, H. Habazaki, A tracer investigation of chromic acid anodizing of aluminium, Surf. Interface Anal., 39 (2007) 860-864.
[20] S.J. Garcia-Vergara, P. Skeldon, G.E. Thompson, T. Hashimoto, H. Habazaki, Compositional evidence for flow in anodic films on aluminum under high electric fields, J. Electrochem. Soc., 154 (2007) C540-C545.
[21] S.J. Garcia-Vergara, P. Skeldon, G.E. Thompson, H. Habazaki, Tracer studies of anodic films formed on aluminium in malonic and oxalic acids, Appl. Surf. Sci., 254 (2007) 1534-1542.
[22] S.J. Garcia-Vergara, P. Skeldon, G.E. Thompson, H. Habazaki, A flow model of porous anodic film growth on aluminium, Electrochim. Acta, 52 (2006) 681-687.
[23] N. Sato, A theory for breakdown of anodic oxide films on metals, Electrochim. Acta, 16 (1971) 1683-1692.
[24] D. Kowalski, J. Mallet, S. Thomas, J. Rysz, B. Bercu, J. Michel, M. Molinari, Self-organization of TiO2 nanotubes in mono-, di- and tri-ethylene glycol electrolytes, Electrochim. Acta, 204 (2016) 287-293.
[25] D. Kowalski, J. Mallet, J. Michel, M. Molinari, Low electric field strength self-organization of anodic TiO2nanotubes in diethylene glycol electrolyte, J. Mater. Chem. A, 3 (2015) 6655-6661.
[26] H. Masuda, M. Yotsuya, M. Asano, K. Nishio, M. Nakao, A. Yokoo, T. Tamamura, Self-repair of ordered pattern of nanometer dimensions based on self-compensation properties of anodic porous alumina, Appl. Phys. Lett., 78 (2001) 826-828.
[27] Y. Bai, L.W. Yang, F. Wu, C. Wu, S. Chen, L.Y. Bao, W.L. Hu, High performance FeFx/C composites as cathode materials for lithium-ion batteries, Journal of Renewable and Sustainable Energy, 5 (2013).
[28] L.P. Li, J.H. Zhu, M.W. Xu, J. Jiang, C.M. Li, In Situ Engineering Toward Core Regions: A

Smart Way to Make Applicable FeF3@Carbon Nanoreactor Cathodes for Li-Ion Batteries, Acs Applied Materials & Interfaces, 9 (2017) 17992-18000.
[29] A.P. Grosvenor, B.A. Kobe, M.C. Biesinger, N.S. McIntyre, Investigation of multiplet splitting of Fe 2p XPS spectra and bonding in iron compounds, Surf. Interface Anal., 36 (2004) 1564-1574.
[30] M.C. Biesinger, B.P. Payne, A.P. Grosvenor, L.W.M. Lau, A.R. Gerson, R.S. Smart, Resolving surface chemical states in XPS analysis of first row transition metals, oxides and hydroxides: Cr, Mn, Fe, Co and Ni, Appl. Surf. Sci., 257 (2011) 2717-2730.
[31] R. Thorpe, S. Rangan, R. Whitcomb, A.C. Basaran, T. Saerbeck, I.K. Schuller, R.A. Bartynski, The solid state conversion reaction of epitaxial FeF2(110) thin films with lithium studied by angle-resolved X-ray photoelectron spectroscopy, PCCP, 17 (2015) 15218-15225.
[32] H.S. Shim, J.W. Kim, Y.E. Sung, W.B. Kim, Electrochromic properties of tungsten oxide nanowires fabricated by electrospinning method, Sol. Energy Mater. Sol. Cells, 93 (2009) 2062-2068.
[33] S.V. Green, A. Kuzmin, J. Purans, C.G. Granqvist, G.A. Niklasson, Structure and composition of sputter-deposited nickel-tungsten oxide films, Thin Solid Films, 519 (2011) 2062-2066.
[34] G.J. He, J.M. Li, W.Y. Li, B. Li, N. Noor, K.B. Xu, J.Q. Hu, I.P. Parkin, One pot synthesis of nickel foam supported self-assembly of NiWO4 and CoWO4 nanostructures that act as high performance electrochemical capacitor electrodes, Journal of Materials Chemistry A, 3 (2015) 14272-14278.
[35] N.V. Alov, XPS study of MoO3 and WO3 oxide surface modification by low-energy Ar+ ion bombardment, physica status solidi c, 12 (2015) 263-266.
[36] C. Bittencourt, M.P. Felicissimo, A. Felten, L.A.O. Nunes, P. Ivanov, E. Llobet, J.J. Pireaux, L. Houssiau, Characterization of WO3 : Ag films: ToF-SIMS studies of ammonia adsorption, Appl. Surf. Sci., 250 (2005) 21-28.
[37] S.J. Garcia-Vergar, I.S. Molchan, F. Zhou, H. Habazaki, D. Kowalski, P. Skeldon, A.E. Thompson, Incorporation and migration of phosphorus species within anodic films on an Al-W alloy, Surf. Interface Anal., 43 (2011) 893-902.
[38] D. Kowalski, Y. Aoki, H. Habazaki, High Proton Conductivity in Anodic ZrO2/WO3 Nanofilms, Angew. Chem., Int. Ed., 48 (2009) 7582-7585.
[39] T.P. Hoar, N.F. Mott, A Mechanism for the Formation of Porous Anodic Oxide Films on Aluminium, J. Phys. Chem. Solids, 9 (1959) 97-99.
[40] J.E. Houser, K.R. Hebert, The role of viscous flow of oxide in the growth of self-ordered porous anodic alumina films, Nature Materials, 8 (2009) 415-420.
[41] P. Skeldon, G.E. Thompson, S.J. Garcia-Vergara, L. Iglesias-Rubianes, C.E. Blanco-Pinzon, A tracer study of porous anodic alumina, Electrochem. Solid-State Lett., 9 (2006) B47-B51.
[42] H. Jung, J. Hwang, H. Chun, B. Han, Elucidation of hydrolysis reaction mechanism of tungsten hexafluoride (WF6) using first-principles calculations, Journal of Industrial and Engineering Chemistry, (2018).
[43] D.R. Lide, CRC Handbook of Chemistry and Physics, 84th Edition, CRC Press2003.
[44] Y. Kajikawa, T. Tsumura, S. Noda, H. Komiyama, Y. Shimogaki, Nucleation of W during chemical vapor deposition from WF6 and SiH4, Japanese Journal of Applied Physics Part 1-Regular Papers Brief Communications & Review Papers, 43 (2004) 3945-3950.

Figure captions:

Figure 1 Current-time (*j-t*) responses for anodizing of sputter deposited (a) Fe and (b) Fe-W (9 at.%) alloy at 40 V, 50 V and 60 V in an ethylene glycol electrolyte containing 1.5 mol dm^{-3} of water and 0.1 mol dm^{-3} of NH_4F at room temperature.

Figure 2 Cross-section SEM images of nanopores/nanotubes formed by anodizing of Fe-W alloy at 40, 50 and 60 V. The anodic layer formed on pure Fe at 60 V is shown as a reference. The metal/alloy layers were anodized in ethylene glycol electrolyte containing 1.5 mol dm^{-3} of water and 0.1 mol dm^{-3} of NH_4F at room temperature.

Figure 3 Surface morphology images for (a,e) as deposited Fe and Fe-W alloys, (b-d) Fe and (f-h) Fe-W (9 at.%) alloy anodized at 40-60 V in ethylene glycol electrolyte containing 1.5 mol dm^{-3} of water and 0.1 mol dm^{-3} of NH_4F at room temperature.

Figure 4 Glow discharge optical emission spectroscopy (GDOES) depth profiles for anodic layers formed at 60 V on a) pure Fe and b) Fe-W alloy.

Figure 5 Fe2p, F1s, O1s, W4f and C1s core level spectra for a) pure Fe anodized at 60V, b) Fe-W alloy anodized at 60 V. Negative ion ToF-SIMS mass spectra (c,d) and depth profile (e) for Fe-W alloy anodized at 60V for 300s in ethylene glycol electrolyte containing 1.5 mol dm^{-3} of water and 0.1 mol dm^{-3} of NH_4F at room temperature.

Figure 6 High angle annular dark field (HAADF) images of FIB lamella for Fe-W alloy anodized at 60 V in ethylene glycol electrolyte containing 1.5 mol dm^{-3} of water and 0.1 mol dm^{-3} of NH_4F at room temperature.

Figure 7 Schematic illustrations for proposed growth of nanopores/nanotubes on a) iron, and b) iron tungsten alloy, c) illustrates post reaction with WF_x compounds leading to formation of thick layer at metal/oxide interface.

Figure 8 Pores size as a function of anodizing voltage for anodic films formed on Fe and Fe-W alloy anodized in ethylene glycol electrolyte containing 1.5 mol dm^{-3} of water and 0.1 mol dm^{-3} of NH_4F at room temperature.

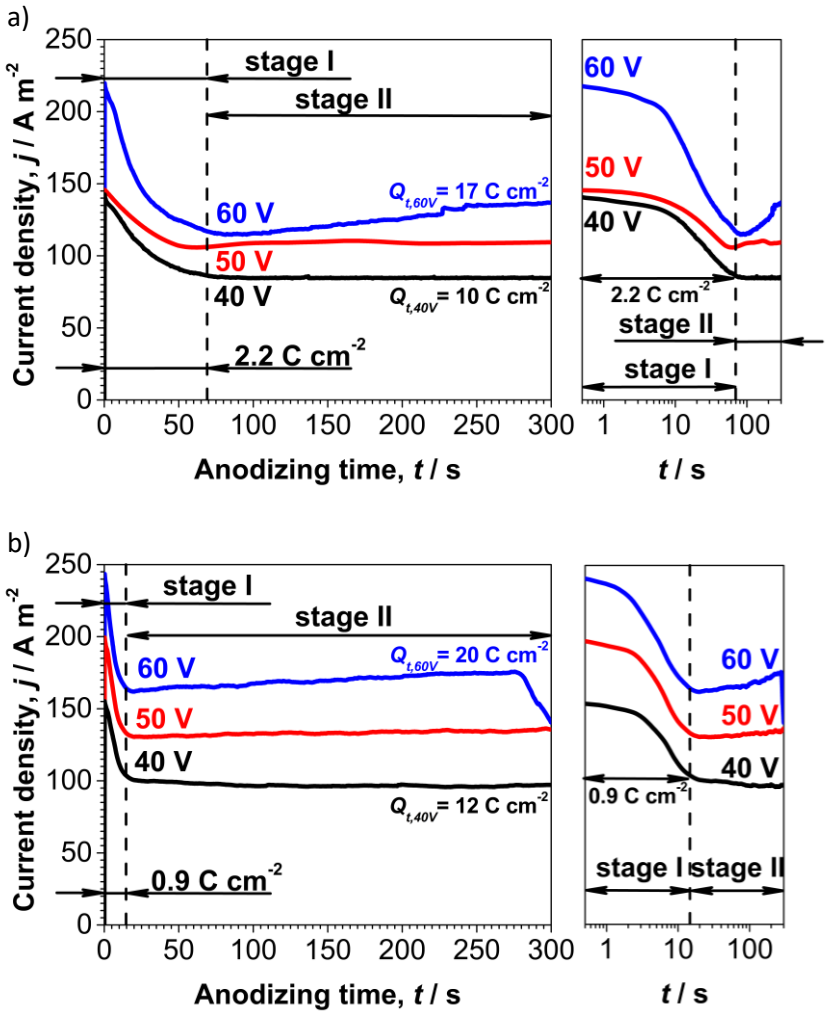

Figure 1 Current-time (*j*-*t*) responses for anodizing of sputter deposited (a) Fe and (b) Fe-W (9 at.%) alloy at 40 V, 50 V and 60 V in an ethylene glycol electrolyte containing 1.5 mol dm^{-3} of water and 0.1 mol dm^{-3} of NH_4F at room temperature.

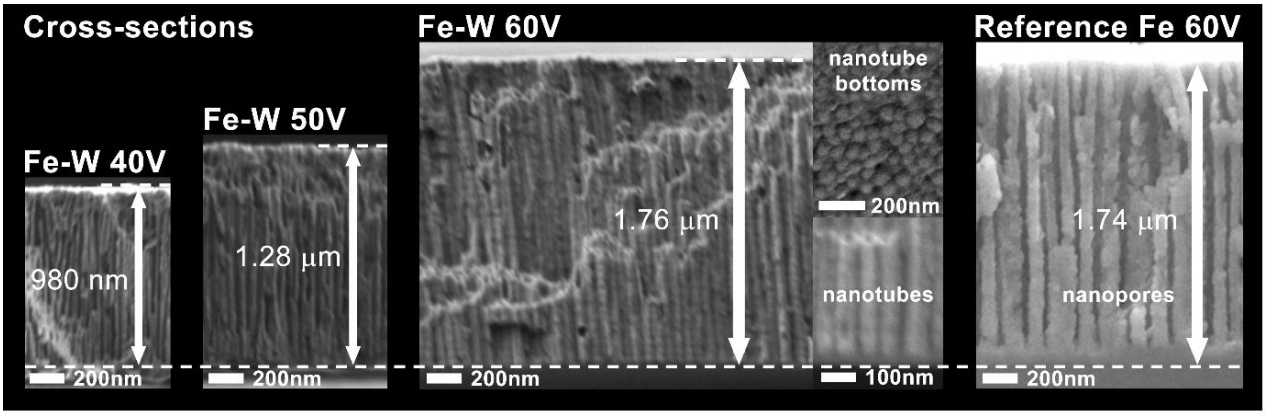

Figure 2 Cross-section SEM images of nanopores/nanotubes formed by anodizing of Fe-W alloy at 40, 50 and 60 V. The anodic layer formed on pure Fe at 60 V is shown as a reference. The metal/alloy layers were

anodized in ethylene glycol electrolyte containing 1.5 mol dm^{-3} of water and 0.1 mol dm^{-3} of NH_4F at room temperature.

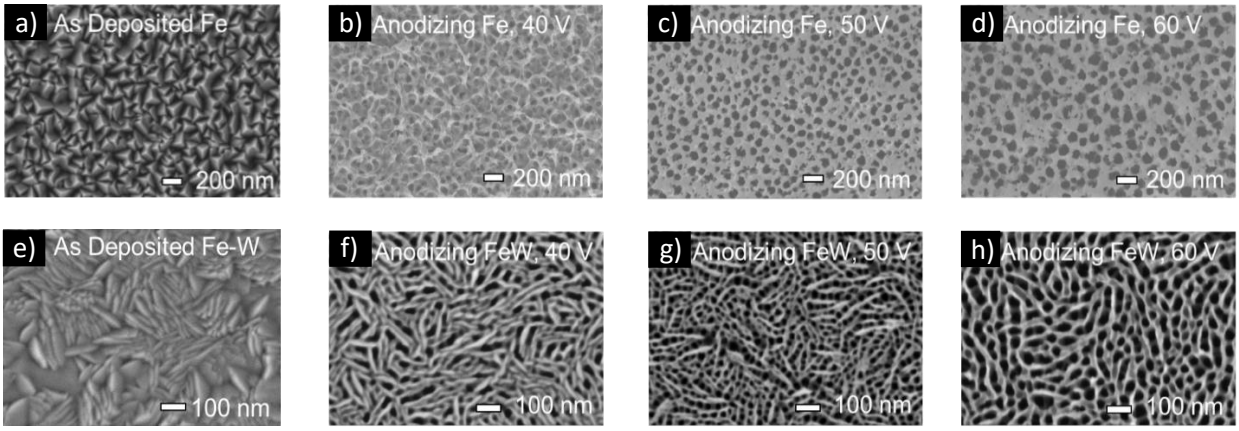

Figure 3 Surface morphology images for (a,e) as deposited Fe and Fe-W alloys, (b-d) Fe and (f-h) Fe-W (9 at.%) alloy anodized at 40-60 V in ethylene glycol electrolyte containing 1.5 mol dm^{-3} of water and 0.1 mol dm^{-3} of NH_4F at room temperature.

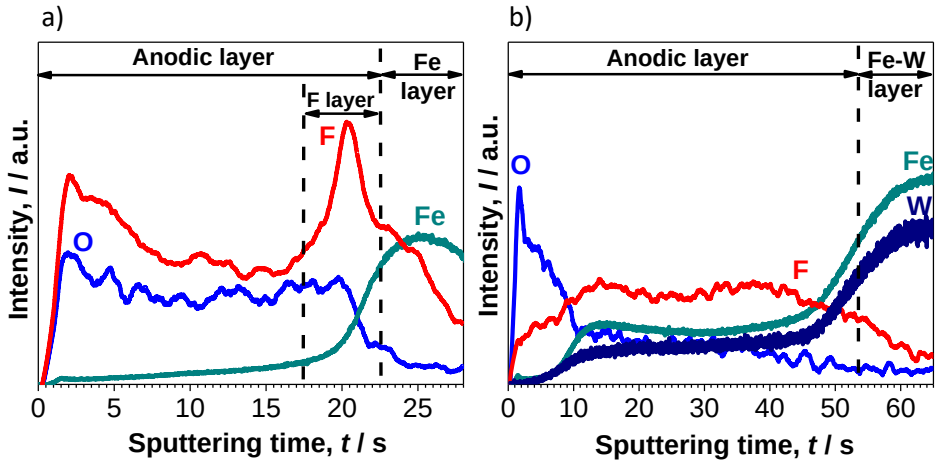

Figure 4 Glow discharge optical emission spectroscopy (GDOES) depth profiles for anodic layers formed at 60 V on a) pure Fe and b) Fe-W alloy.

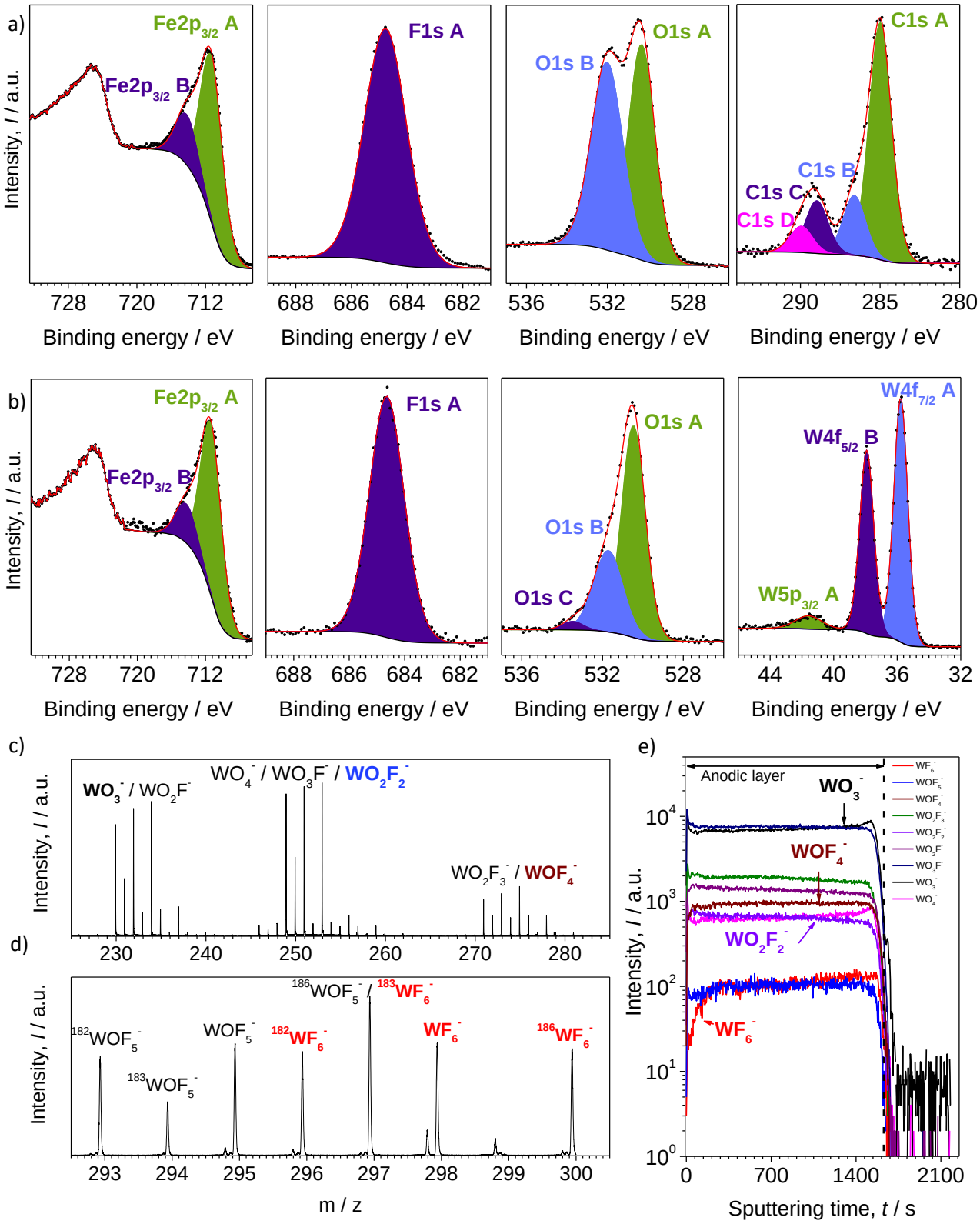

Figure 5 Fe2p, F1s, O1s, W4f and C1s core level spectra for a) pure Fe anodized at 60V, b) Fe-W alloy anodized at 60 V. Negative ion ToF-SIMS mass spectra (c,d) and depth profile (e) for Fe-W alloy anodized

at 60V for 300s in ethylene glycol electrolyte containing 1.5 mol dm^{-3} of water and 0.1 mol dm^{-3} of NH_4F at room temperature.

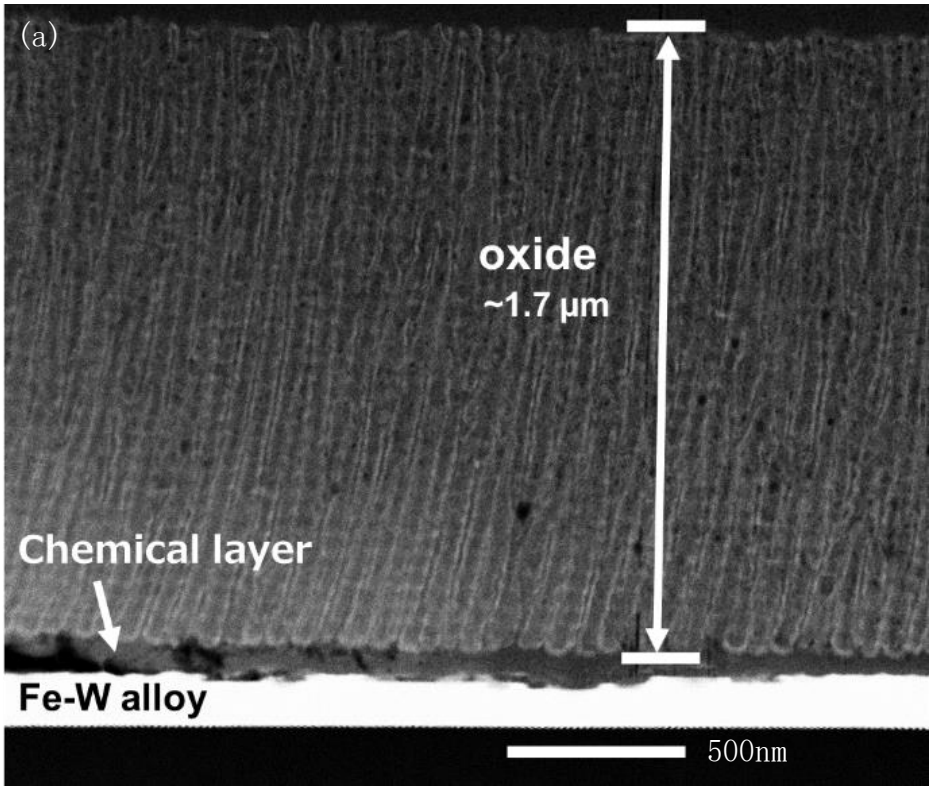
(a)
oxide
~1.7 μm
Chemical layer
Fe-W alloy
500nm

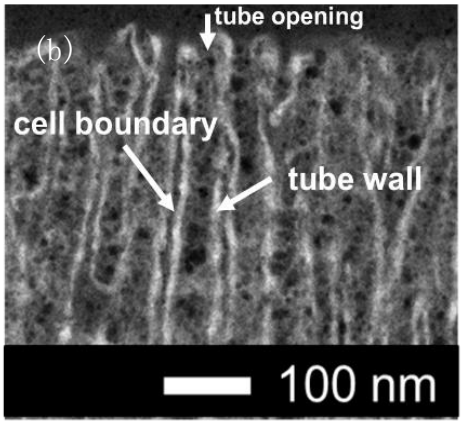
(b)
tube opening
cell boundary
tube wall
100 nm

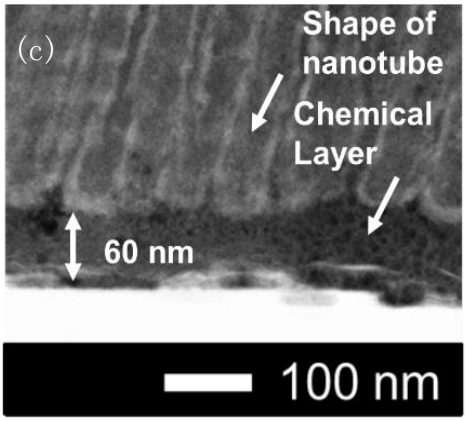
(c)
Shape of nanotube
Chemical Layer
60 nm
100 nm

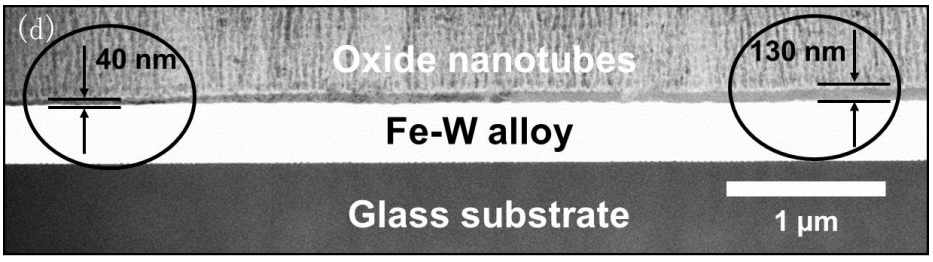
(d)
40 nm
Oxide nanotubes
130 nm
Fe-W alloy
Glass substrate
1 μm

Figure 6 High angle annular dark field (HAADF) images of FIB lamella for Fe-W alloy anodized at 60 V in ethylene glycol electrolyte containing 1.5 mol dm^{-3} of water and 0.1 mol dm^{-3} of NH_4F at room temperature.

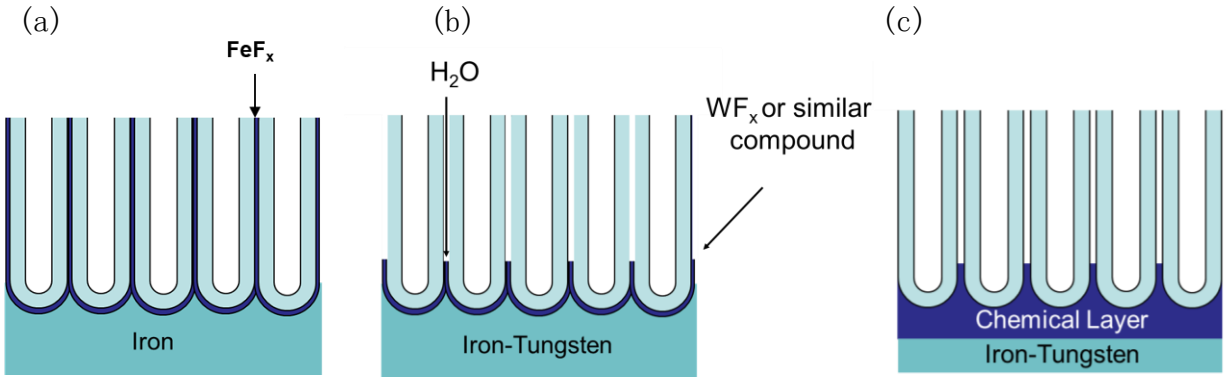

Figure 7 Schematic illustrations for proposed growth of nanopores/nanotubes on a) iron, and b) iron tungsten alloy, c) illustrates post reaction with WF_x compounds leading to formation of thick layer at metal/oxide interface.

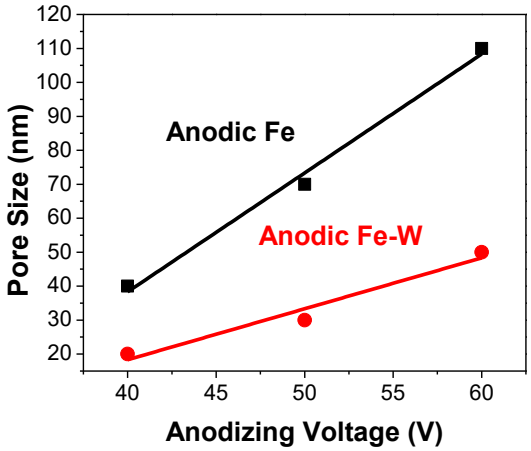

Figure 8 Pores size as a function of anodizing voltage for anodic films formed on Fe and Fe-W alloy anodized in ethylene glycol electrolyte containing 1.5 mol dm^{-3} of water and 0.1 mol dm^{-3} of NH_4F at room temperature.